Supporting Information

Hydrogen-bonded supramolecular biohybrid frameworks for protein biomineralization constructed from natural phenolic building blocks

Qiuping Xie, Yue Wu, Haojie Zhang, Qinling Liu, Yunxiang He,* Ian Manners, and Junling Guo*

Table of Contents

Section S1. General characterizations

CLSM observation

The spatial localization of ProteinX@SPF self-assembled with FITC-labeled BSA was accurately determined using confocal laser scanning microscopy (CLSM; Olympus Lext OLS5000). For fluorescence excitation, the FITC-tagged BSA was illuminated at 488 nm, and the emitted fluorescence signal was captured within a spectral window ranging from 495 to 545 nm. To comprehensively assess the spatial distribution of BSA for 3D visualization and analysis, six z-stacks were acquired for each sample. These z-stacks were captured at incremental depths of 0.2 μm, commencing from the surface (defined as the initial plane where ProteinX@SPF was identifiable).

HR-TEM imaging and simulation

HR-TEM experiments were conducted using a FEI Titan Cube transmission electron microscope, operated at an acceleration voltage of 200 kV. Specimen exploration, zone axis alignment, and prefocusing were performed with a carefully controlled dose rate of approximately 0.01–$0.03\,e\,Å^{-2}\,s^{-1}$. High-resolution TEM images were captured at a magnification of 44,000 using a Gatan K2 direct-detection camera, operating in electron-counting mode and employing a dose fractionation technique. Each image stack comprised 120 frames, with an exposure time of 0.05 s per frame, resulting in a total exposure duration of 6 s and an accumulated electron dose of approximately $4\,e\,Å^{-2}$. Electron diffraction patterns were recorded using a Gatan Ultra-scan charge-coupled device camera.

SAXS experiment

SAXS was employed to investigate the pore structure of ProteinX@SPF. The SAXS experiments were conducted using a Bruker NANOSTAR U SAXS system. Before data acquisition, the specimen was placed in a vacuum-sealed sample chamber, and evacuated to a pressure below 3 mbar, to minimize atmospheric scattering effects on the X-ray beam. Data collection was performed at a fixed sample-to-detector distance (SDD) of 310 mm, utilizing an incident X-ray beam with an energy of 50 keV, a current of 0.6 mA, and a wavelength of 1.54 Å. For each specimen, four frames were averaged, with a total count time of 600 s. Subsequent data analysis involved fitting the SAXS data using the Guinier and Porod models within the SASfit software package (version 0.94.11, Paul Scherrer Institute, Switzerland). This model-independent approach is crucial for SAXS data analysis as it enables the extraction of structural information without requiring prior knowledge of the system. Structural parameters, including those derived from Guinier and Porod fittings, were analyzed using a non-linear least-squares method. The radius of gyration data were directly obtained following the fitting procedure.

DFT calculation

DFT calculations were performed using the gradient-corrected correlation functional wb97xd65, augmented with Grimme's D2 dispersion model, to determine the properties of the complexes. The geometries of complexes comprising an EA molecule and an amino acid residue were optimized at the 6-31+G(d,p) level of theory, incorporating the solvation model based on density (SMD) in a water environment. Vibrational frequencies were computed to

validate the local minimum nature of each structure on the potential energy surface and to derive thermodynamic quantities. The pK$_a$ values were calculated using Equation 1:

$$pK_a = \frac{\Delta G^*_{aq}}{2.303RT}$$

Where ΔG^*_{aq} was precisely determined by directly computing the aqueous Gibbs free energies of both the acid and its conjugate base in the 1M standard state.

To estimate the binding free energies between amino acid residue (A) and EA (B), aspartic acid (Asp) was selected as the representative residue model. The binding free energies were calculated based on Equation 2:

$$\Delta G(AB) = G(AB)_{aq} - (G(A)_{aq} + G(B)_{aq})$$

Where $G(AB)_{aq}$, $G(A)_{aq}$ and $G(B)_{aq}$ were derived from the frequency calculations conducted in a water environment. All electronic structure calculations were executed using Gaussian 16 revision A.03.

Structural simulations of ProteinX@SPF were performed using the Reflex Plus module in Materials Studio (version 8.0) by Accelrys Inc. The initial models were initially crafted in a segmented manner, commencing with a triclinic unit cell belonging to the $P1$ space group. The estimations for the values of a and c were derived from the geometry and dimensions of the constituent building blocks, and subsequently refined through indexing the experimental peak positions obtained from PXRD analysis. For an accurate whole-profile fitting, the Pseudo-Voigt function was adopted, while the Berrar-Baldinozzi function served as a tool for correcting asymmetries during the refinement process.

QCM analysis

QCM was employed to monitor the binding of EA onto a physisorbed surface of the protein. Initially, a pristine gold surface was coated with BSA at a concentration of 1 mg ml^{-1} in phosphate buffer (0.1 M NaPi, pH 7.4) until saturation was achieved. Subsequently, a stable baseline was established by flowing phosphate buffer alone, without BSA, through the system. Subsequently, a solution of EA, dissolved in phosphate buffer and filtered through a 0.22 μm filter, was pumped through the measurement chambers at a flow rate of 0.05 ml min^{-1}. Once the signal stabilized, pure phosphate buffer was again flowed through the chambers.

Catalytic measurement

The catalytic performance of GOx@SPF was rigorously evaluated by monitoring the production of H$_2$O$_2$ through an enzymatic assay employing horseradish peroxidase (HRP). Specifically, the concentration of GOx was standardized at 50 μg ml^{-1} in each experiment, while the quantity of GOx@SPF was determined based on enzyme loading calculations using the Bradford assay. The GOx@SPF was dispersed in 0.1 ml of tris buffer (pH 7.5, 50 mM) containing 5 mg of HRP, followed by the addition of 0.2 ml of the prepared ODA solution as the hydrogen donor. Subsequently, 0.2 ml of a glucose standard was promptly added to initiate the catalytic reaction. The production of H$_2$O$_2$ quantitatively oxidized ODA to a red ODA$^{\bullet+}$,

which was monitored at 436 nm using a UV-vis spectrophotometer in a time-scanning mode.

The catalytic performance of CAT@SPF was evaluated by tracking the depletion of H_2O_2. In these experiments, the concentration of CAT was maintained at 50 μg ml^{-1}, with the dosage of CAT@SPF determined using enzyme loading calculations from the Bradford assay. CAT@SPF was dispersed into 0.1 ml of tris buffer (pH 7.5, 50 mM) and pre-incubated at 25 °C for 30 min. Immediately after, 5 ml of an aqueous hydrogen peroxide solution (20 mM) was added to initiate the catalytic reaction. The depletion of H_2O_2 was tracked at 240 nm using a UV-vis spectrophotometer in a time-scanning mode.

The selective catalysis of LIP@SPF was conducted using the spectrometric method, employing methyl formate (MF) and cholesterol formate (CF) as substrates. Initially, MF and CF were dissolved in a pH 7.4 Tris-HCl/ethanol (1:3) solution to prepare the substrate mixture. Subsequently, 500 µL of LIP@SPF solution was added to 100 µL of the substrate solution. Throughout the experiments, the LIP concentration was maintained at 200 µg ml^{-1}, while the CAT@SPF dosage was determined using enzyme loading calculations derived from the Bradford assay. The hydrolysis of MF and CF yielded formic acid (HCOOH), which was detected at 205 nm using a UV-Vis spectrophotometer and quantitatively analyzed via a standard calibration curve.

Section S2. Supporting figures
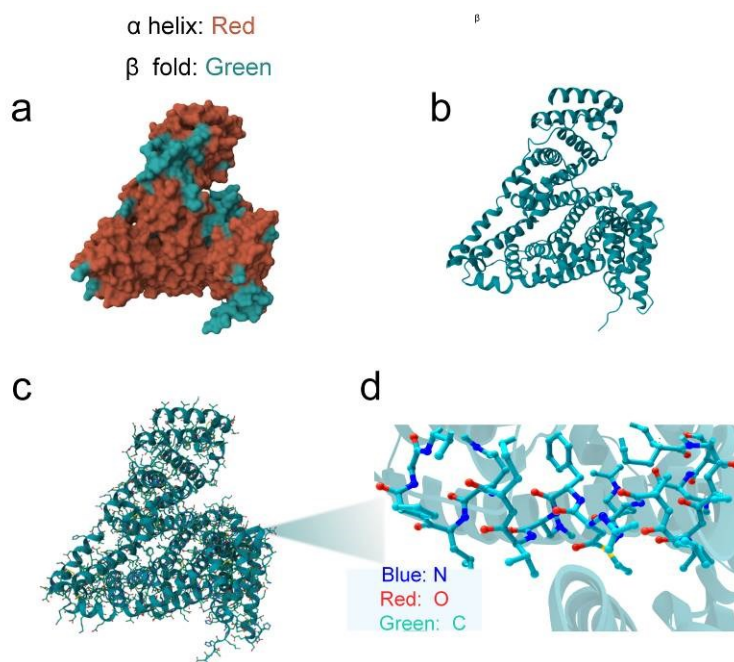
Fig. S1. Structure of BSA. The structure of BSA is presented in various modes: (a) Coarse surface representation. (b) Polymer cartoon view with peptide skeleton outlined. (c) Atomic-level detail. (d) Enlarged view of the atomic detail in (c). The BSA structural data was retrieved from the Protein Data Bank (DOI: 10.2210/pdb4F5S/pdb).
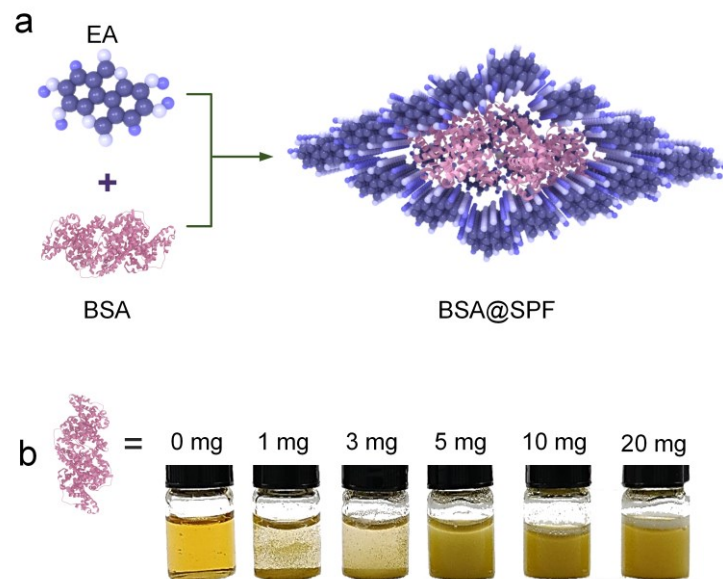
Fig. S2. (a) Self-assembly illustration of the BSA@SPF. (b) Photographic record of the self-assembly process by using different protein dosages, along with the corresponding transmittance after a reaction period of 30 min. The solution gradually became turbid with the increase in dosage of BSA, illustrating the successful self-assembly of BSA@SPF.
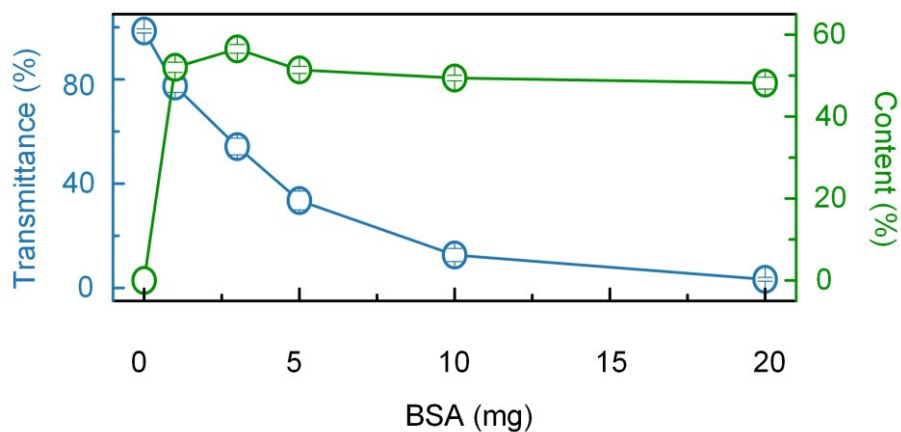
Fig. S3. The transmittance and corresponding protein content of BSA@SPF by self-assembling EA with different dosages of BSA. The transmittance of the solution decreased and the content of BSA displayed a dynamic increasing trend with the increase of BSA dosage, illustrating the successful self-assembly of BSA@SPF.
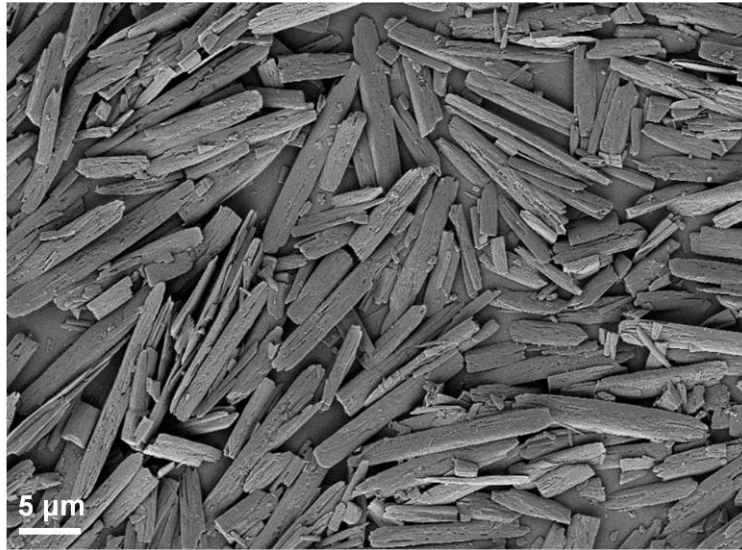
Fig. S4. SEM image of BSA@SPF. SEM image of the BSA@SPF showed the rod-like structure.
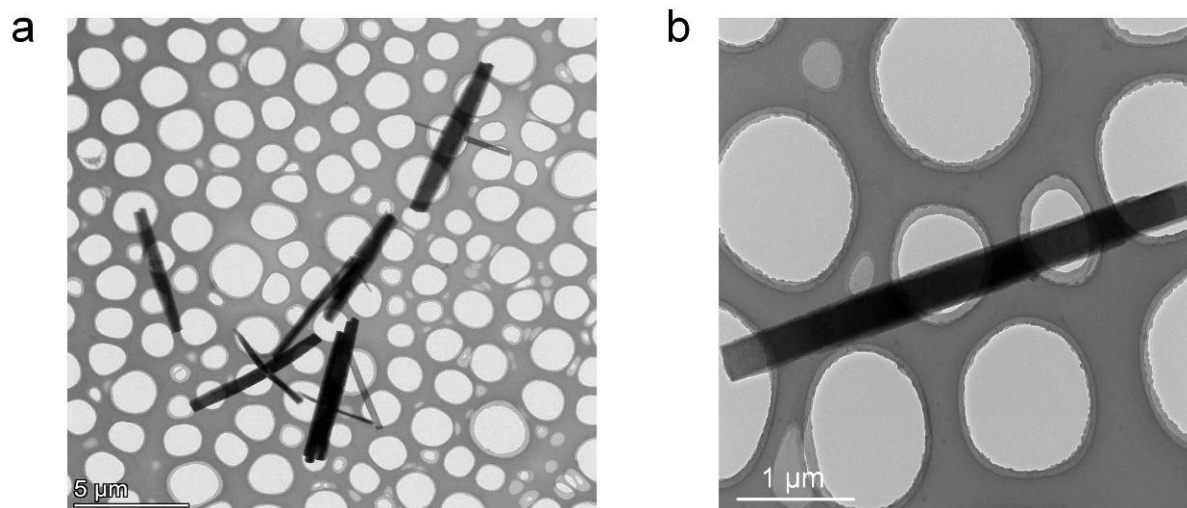
Fig. S5. TEM image (a) and enlarged area (b) of BSA@SPF. TEM image of the BSA@SPF showed the rod-like structure.
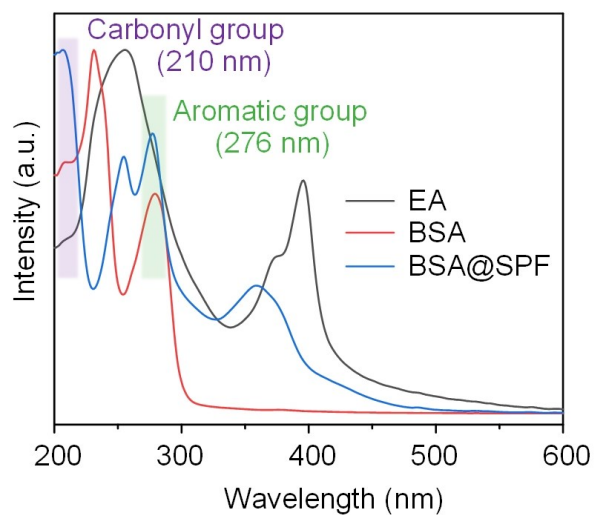
Fig. S6. UV-Vis spectra of EA, BSA and BSA@SPF, respectively. The peaks for amide groups (210 nm) and aromatic groups (276 nm) confirmed the existence of BSA in BSA@SPF.
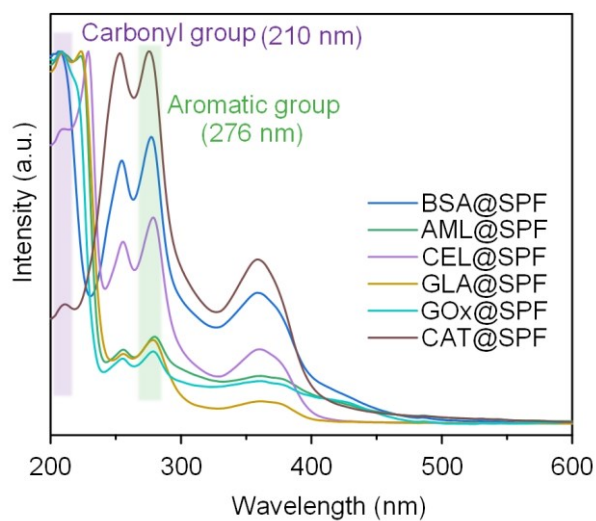
Fig. S7. UV-Vis spectra of ProteinX@SPF with various proteins. The peaks for amide groups (210 nm) and aromatic groups (276 nm) confirmed the existence of protein in ProteinX@SPF.
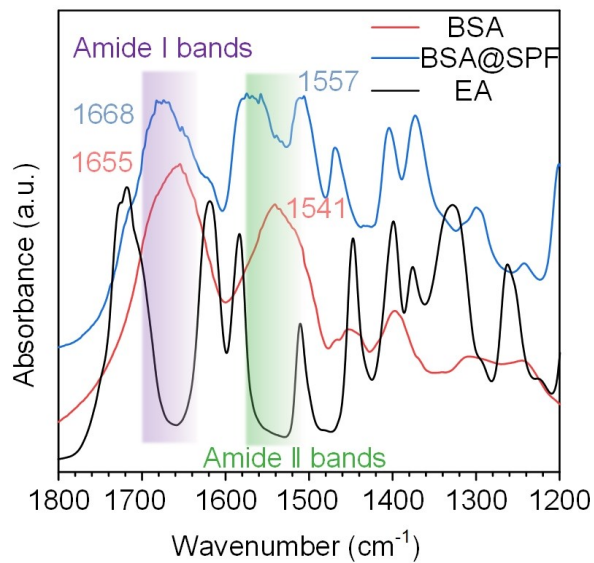
Fig. S8. FT-IR spectra of EA, BSA, and BSA@SPF, respectively. The peaks for amide I (1655–1668 cm^{-1}) and amide II bands (1541–1557 cm^{-1}) confirmed the existence of BSA in the BSA@SPF. Additionally, compared with free BSA, BSA@SPF displayed a blue shift of these peaks in FT-IR spectra, illustrating the high dispersibility of BSA due to the self-assembly process.
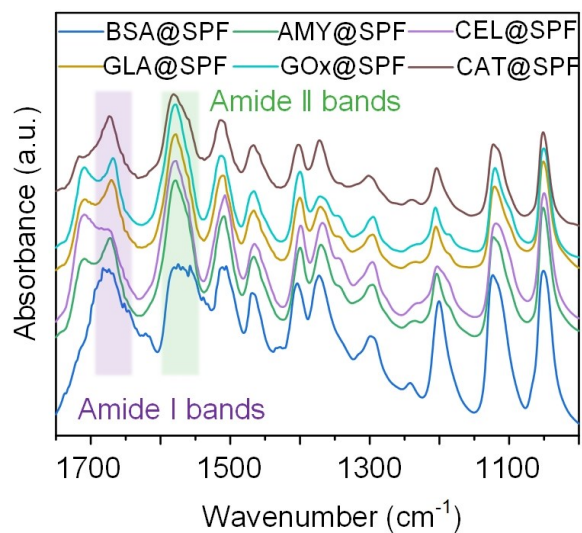
Fig. S9. FT-IR spectra of ProteinX@SPF with various proteins. The peaks for amide I (1655–1668 cm^{-1}) and amide II bands (1541–1557 cm^{-1}) confirmed the existence of protein in the ProteinX@SPF.
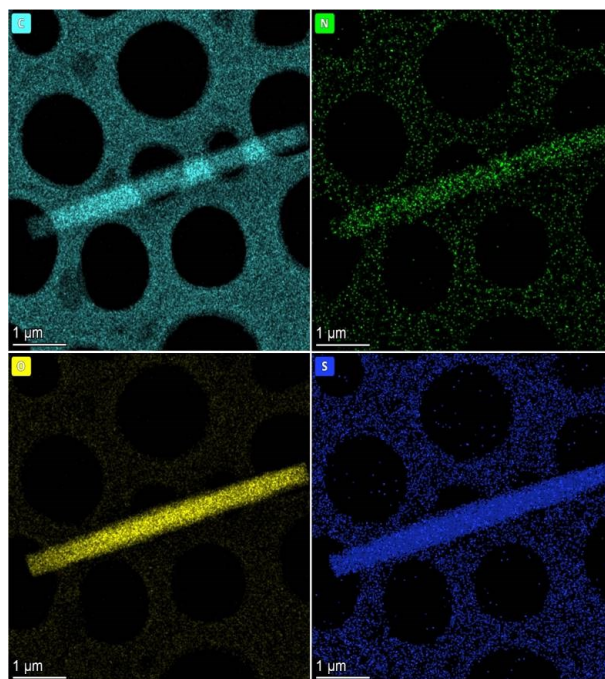
Fig. S10. EDS elemental mapping images of BSA@SPF. The uniform distribution of each element including C, N, O, and S in EDS mapping manifested the existence of BSA in the BSA@SPF.
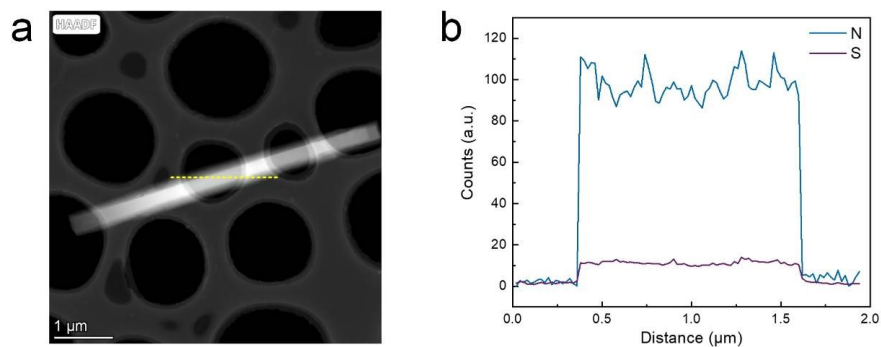
Fig. S11. HADDF-STEM image (a) and corresponding EDX spectra (b) of BSA@SPF. The uniform distribution of proteins was confirmed by the well-dispersed N and S elements attributed to the proteins.
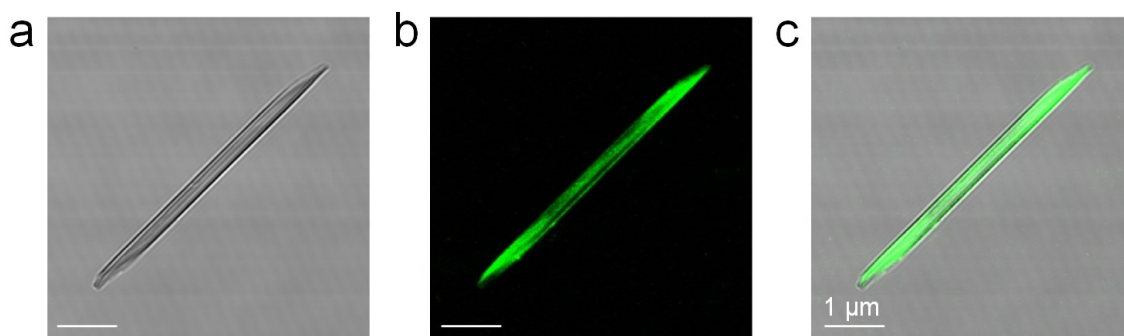
Fig. S12. The bright field (a), dark field (b), and merged (c) CLSM images of the BSA$_{FITC}$@SPF excited at 488 nm. The uniform distribution of green fluorescence indicated the homogenous dispersion of BSA$_{FITC}$ within the BSA$_{FITC}$@SPF.
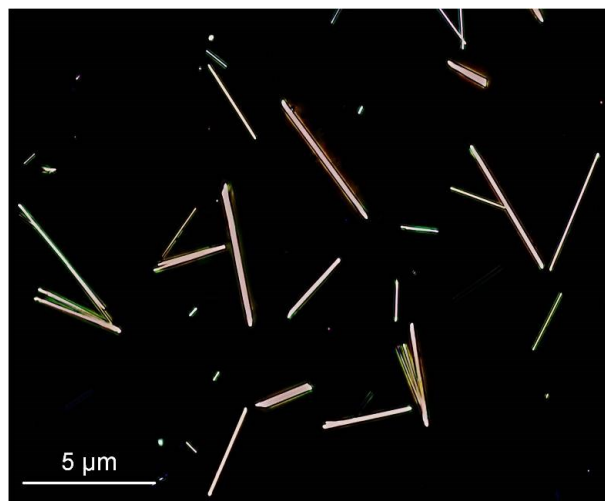
Fig. S13. Polarized optical microscopy image of BSA@SPF. The presence of strong birefringence demonstrated the inherent crystallinity of BSA@SPF.
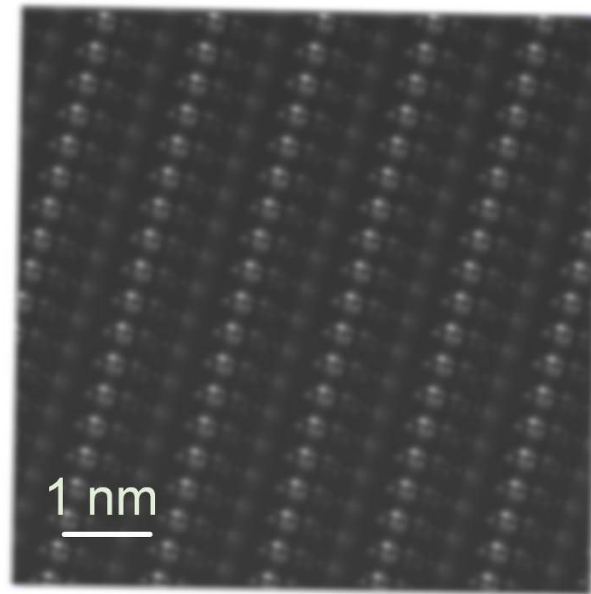
Fig. S14. The simulated HR-TEM image according to the model of ProteinX@SPF. The simulated HR-TEM image exhibited a notable consistency with the experimental HR-TEM image, further validating the reliability of the ProteinX@SPF model.
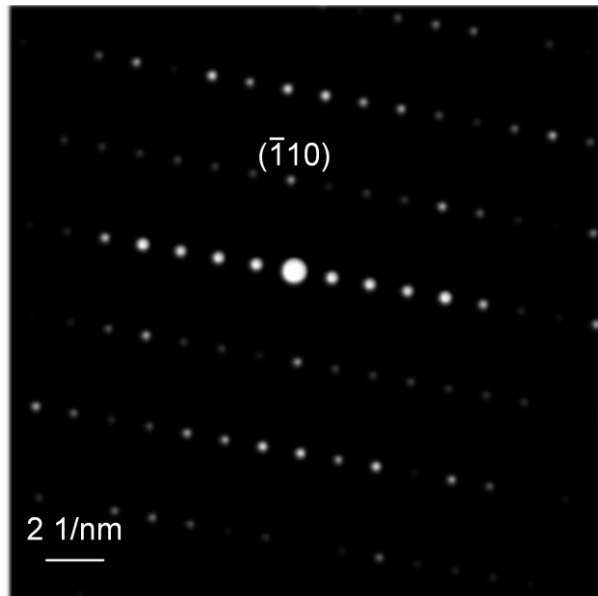
Fig. S15. The simulated SAED pattern according to the model of ProteinX@SPF. The simulated SAED pattern, derived from the ProteinX@SPF model, demonstrated remarkable agreement with the experimental SAED pattern, thereby strengthening the credibility of the ProteinX@SPF model.
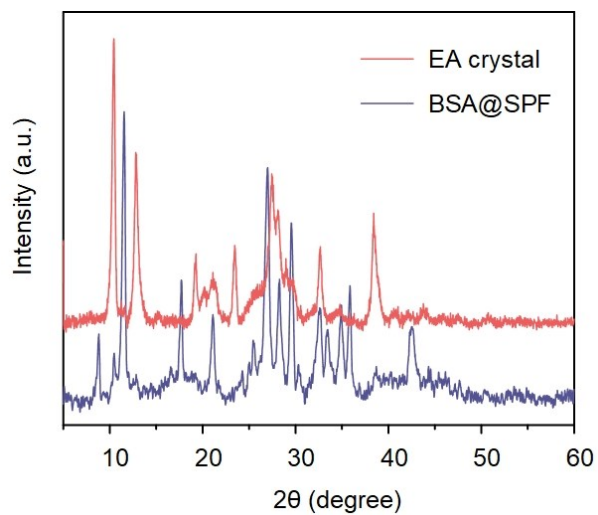
Fig. S16. The experimental XRD pattern of EA crystal and BSA@SPF. The XRD pattern of the EA crystal differed from that of BSA@SPF, indicating distinct lattice structures between EA crystal and BSA@SPF.
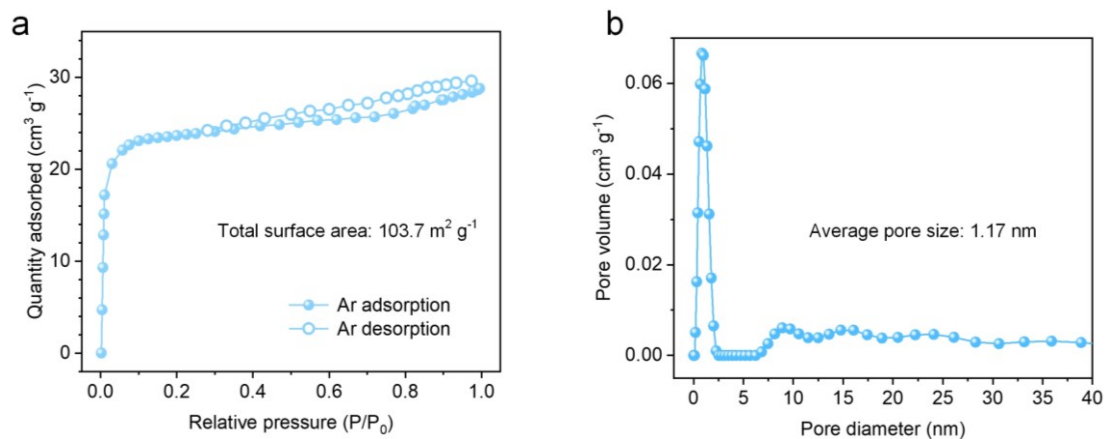
Fig. S17. Argon adsorption/desorption isotherms (a) and pore size distribution analysis of BSA@SPF. The results revealed a relatively high surface area of 103.7 m² g⁻¹ and an average pore size of 1.17 nm, confirming the porous structure of BSA@SPF.
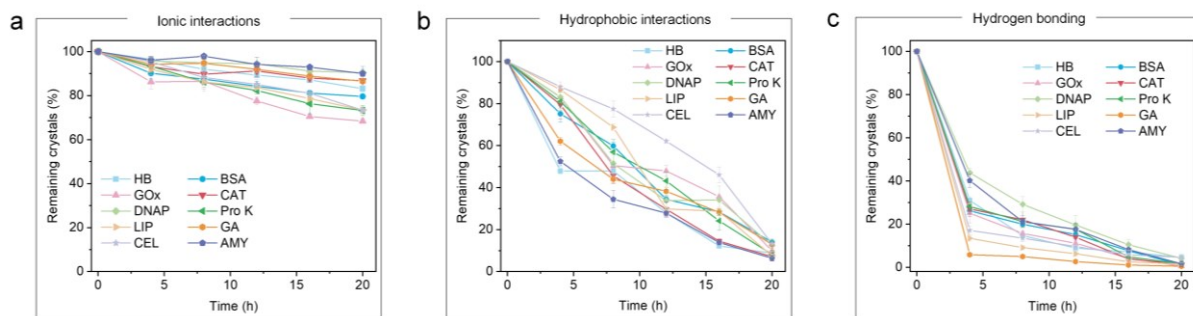
Fig. S18. Interaction-dependent degradability kinetics of ProteinX@SPF with various proteins in the presence of 100 mM NaCl (a), 100 mM Tween 20 (b), or 100 mM urea (c), as evaluated using optical microscopy. The data were presented as mean ± standard deviation (N = 3).
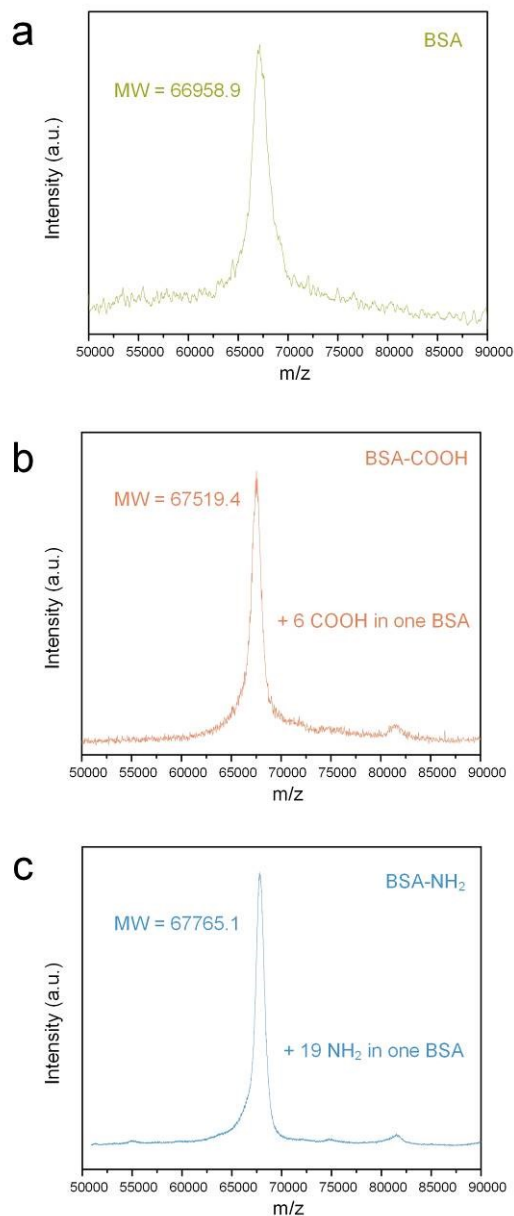
Fig. S19. MALDI-TOF/TOF-MS profiles of the molecular weights of BSA (a), BSA-COOH (b), and BSA-NH₂ (c), respectively. The results indicated the successful introduction of approximately 6 -COOH groups and 19 -NH₂ groups onto each BSA molecule through succinylation and amination, respectively.
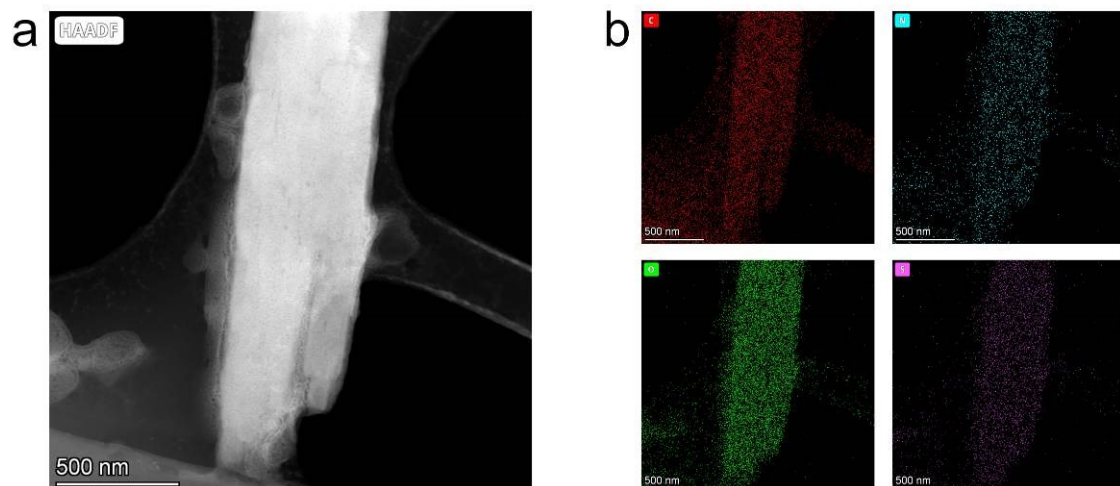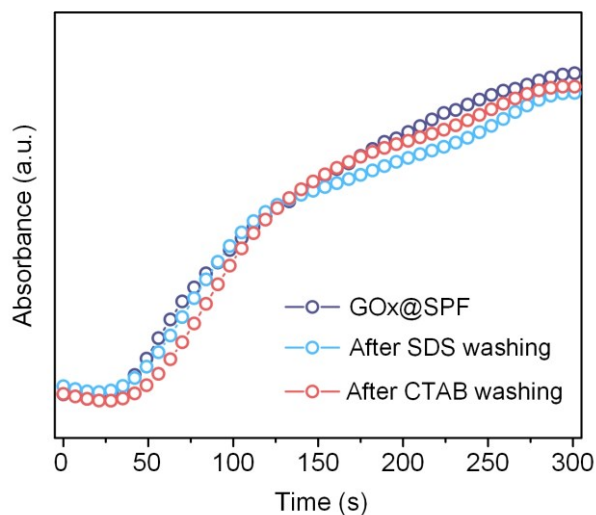
Fig. S20. HAADF-STEM image (a) and the corresponding EDS mapping images (b) of GOx@SPF. The uniform distribution of each element including C, N, O, and S in EDS mapping manifested the existence of GOx in GOx@SPF.
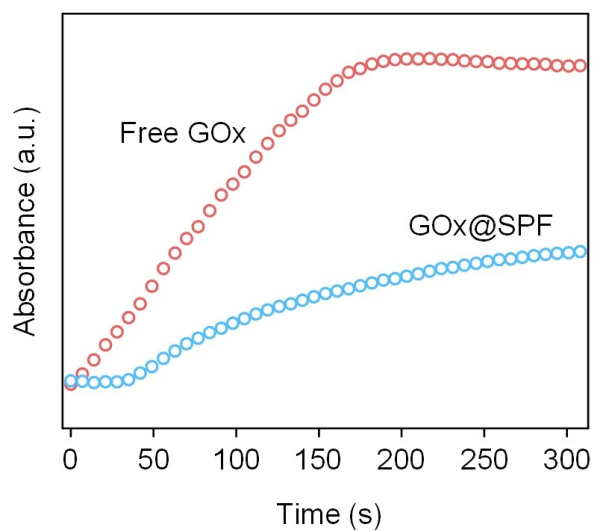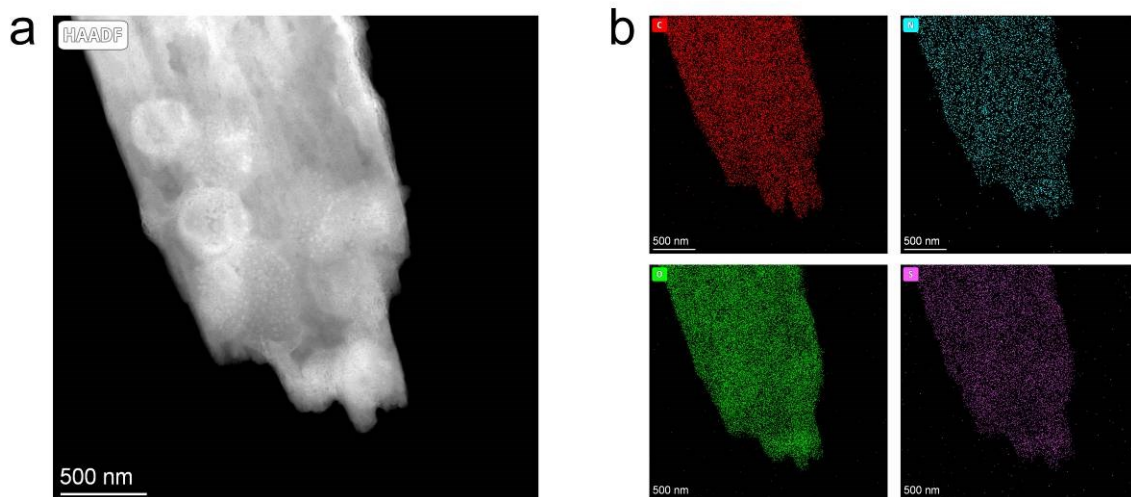
Fig. S21. Catalytic kinetics of free GOx and GOx@SPF. The descending trend observed in the curves of free GOx and GOx@SPF demonstrated the successful catalytic conversion of glucose by GOx.
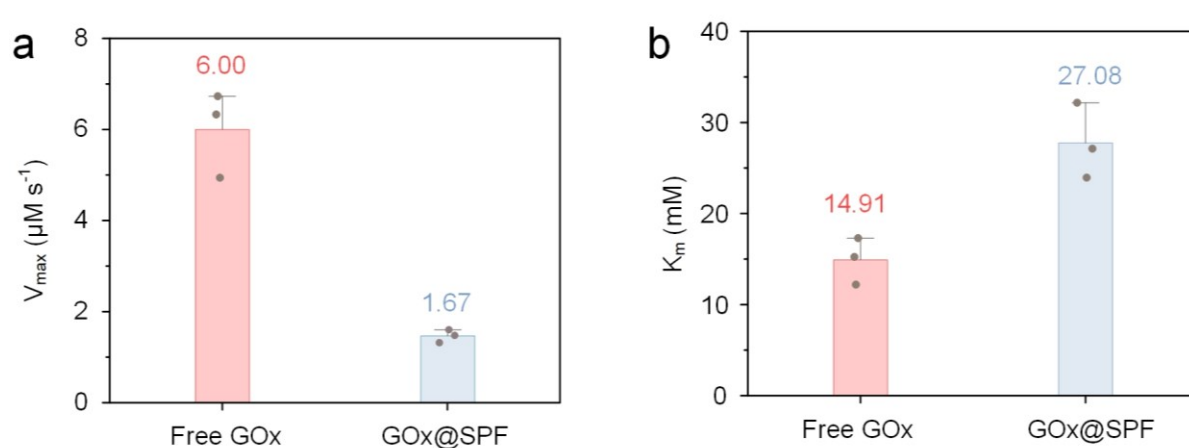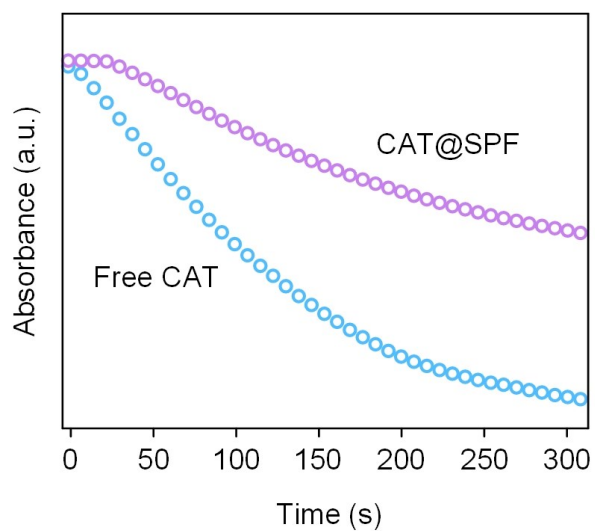
Fig. S22. The evaluated values of maximum catalytic rate (V_{max}, a) and Michaelis-Menten constant (K_m, b) in free GOx and GOx@SPF. GOx@SPF exhibited a V_{max} of 1.67 μM s^{-1}, illustrating the reserved biocatalytic activity of assembled GOx in GOx@SPF. The higher K_m of GOx@SPF (27.08 mM) compared with free GOx (14.91 mM) suggested the size-restricted diffusion of GOx@SPF.

Fig. S23. Catalytic kinetics of GOx@SPF after washing with SDS or CTAB. The catalytic kinetics of GOx@SPF following washing with SDS or CTAB showed similar trends in the curves compared to pristine GOx@SPF, indicating that the catalytic ability of GOx@SPF primarily derives from the encapsulated proteins rather than those bound to the surface.
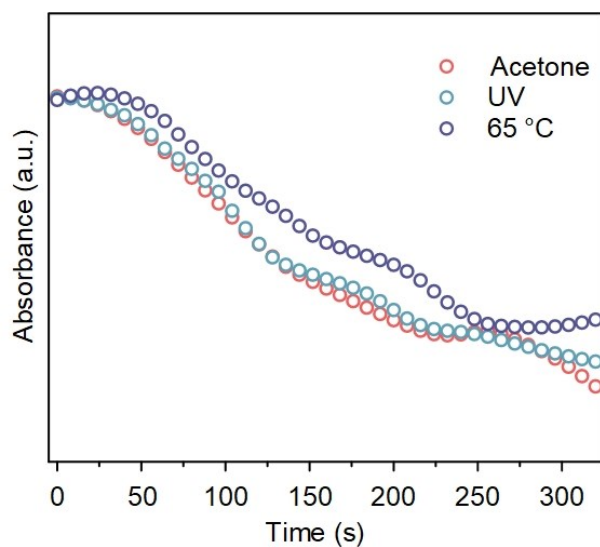
Fig. S24. HAADF-STEM image (a) and the corresponding EDS mapping images (b) of CAT@SPF. The uniform distribution of each element including C, N, O, and S in EDS mapping manifested the existence of CAT in CAT@SPF.

Fig. S25. Catalytic kinetics of free CAT and CAT@SPF. The descending trend observed in the curves of free CAT and CAT@SPF demonstrated the successful catalytic conversion of H_2O_2 by CAT.
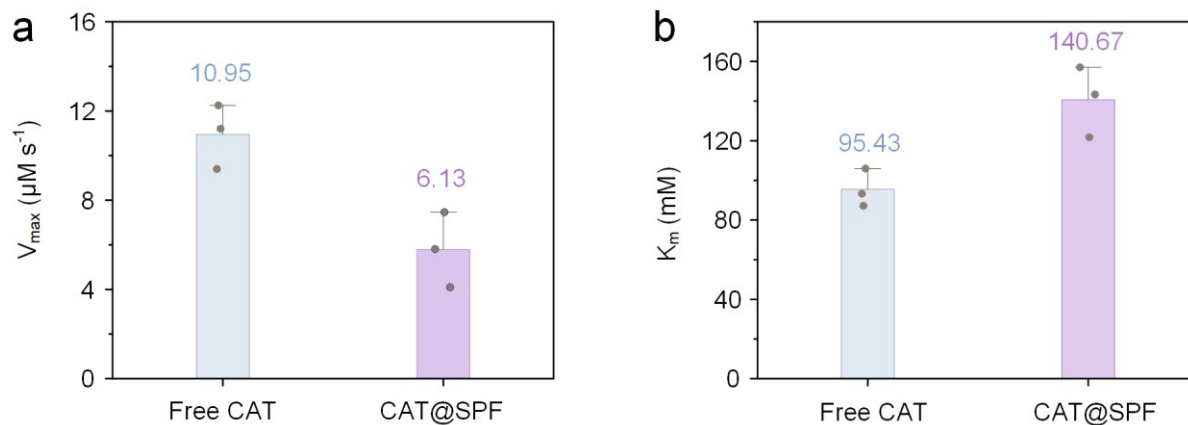
Fig. S26. The evaluated values of V_{max} (a) and K_m (b) in free CAT and CAT@SPF. CAT@SPF exhibited a V_{max} of 6.13 μM s^{-1}, illustrating the reserved biocatalytic activity of assembled CAT in CAT@SPF. The higher K_m value of CAT@SPF (140.67 mM) compared to free CAT (95.43 mM) suggested a size-restricted diffusion within CAT@SPF.

Fig. S27. Catalytic kinetics of CAT@SPF after the treatment of organic solvent (acetone), radiation (UV), and heating (65 ℃), respectively. It was revealed that CAT@SPF retained a significant portion of its biocatalytic ability, indicating its stability under harsh conditions.
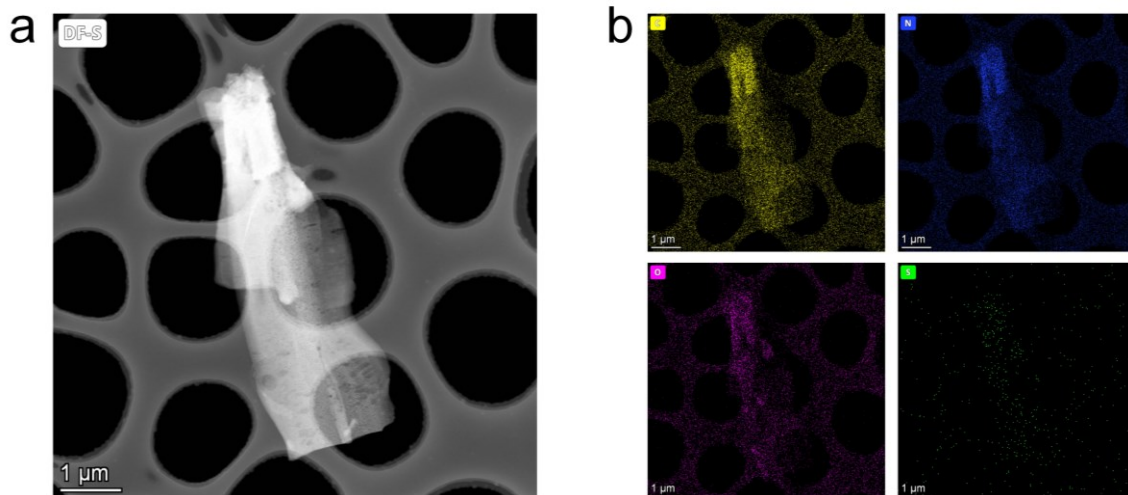
Fig. S28. HAADF-STEM image (a) and the corresponding EDS mapping images (b) of LIP@SPF. The uniform distribution of each element including C, N, O, and S in EDS mapping manifested the existence of LIP in LIP@SPF.
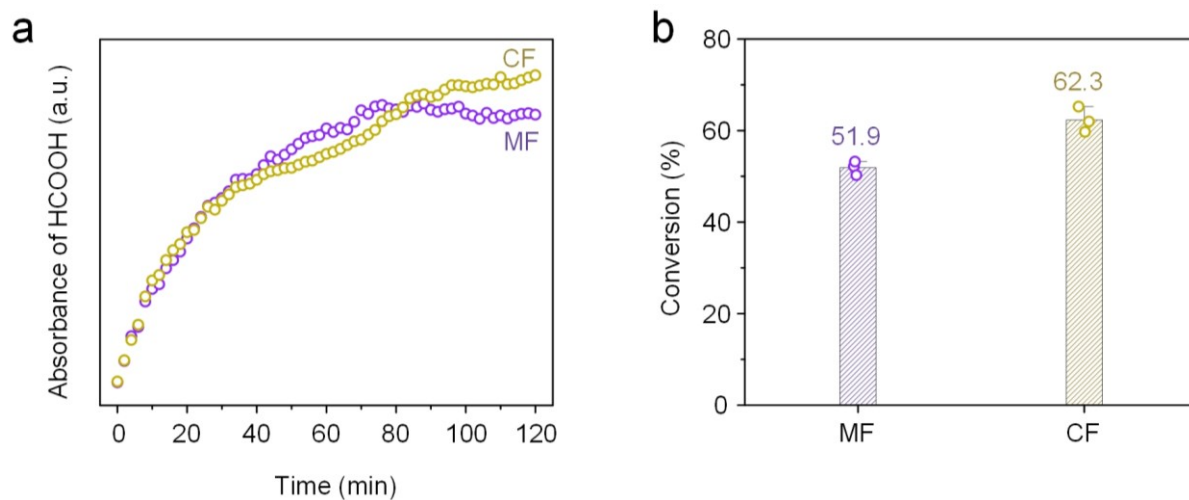
Fig. S29. The catalytic kinetics (a) and conversion efficiency (b) of free LIP. Comparable kinetic values and conversion efficiency between MF and CF indicated the non-specific catalytic performance of free LIP for MF and CF.

Section S3. Supporting tables

Table S1. The protein loading contents of ProteinX@SPF using various proteins as building blocks

10 mg proteins	Loaded proteins (mg)	Loading contents (%)	Loading contents after SDS washing (%)	Loading contents after CTAB washing (%)
AMY	5.22	52.2	49.1	50.4
CEL	8.81	88.1	82.5	84.3
GA	4.88	48.8	46.7	47.1
CAT	4.23	42.3	41.5	39.4
GOx	5.09	50.9	47.3	48.2
BSA	5.65	56.5	54.9	52.1

Table S2. Crystallographic data and refined parameters of ProteinX@SPF.

Name	ProteinX@SPF
Chemical composition	$C_{14}H_6O_8$
Mass formula	302.194
Crystal system	triclinic
Space group	$P1$
a (Å)	11.4496(5)
b (Å)	3.5561(8)
c (Å)	19.1899(7)
α (°)	76.921(7)
β (°)	51.867(2)
γ (°)	88.877(2)
R_p	0.0237
R_{wp}	0.0412
R_{exp}	0.0259
Crystal density (g cm^{-3})	1.714

Table S3. Calculated pK_a of EA.

	EA$_1$[a]	EA$_2$[b]
ΔG_{aq}^{*} (kJ mol^{-1})	53.17	64.30
pK_a	9.31	11.26

[a], [b]: Symmetric phenolic hydroxyl groups of EA in different positions.